Spatial and temporal measurement of recombining detached plasmas by laser Thomson scattering

Shin Kajita

IMaSS, Nagoya University, Nagoya 464-8603, Japan

E-mail: kajita.shin@nagoya-u.jp

Hiroshi Ohshima, Hirohiko Tanaka, Masamichi Seki, Hiroki Takano, and Noriyasu Ohno

Graduate School of Engineering, Nagoya University, Nagoya 464-8603, Japan

Abstract. Elucidation and control of the low temperature recombining plasmas under fusion relevant conditions are crucial issues. In this study, we applied a conditional average for laser Thomson scattering technique to measure the temporal evolution of the plasma instability in detached recombining plasmas in the divertor simulator NAGDIS-II. In recombining plasmas, it is shown that the electron energy distribution function has a non-Maxwellian component, and the fraction of low electron temperature component increases with the gas pressure. It is found that one of the major reasons to cause the non-Maxwellian distribution function is in the temporal variations of the electron temperature. By using the conditional averaging method, the temporal evolutions of the spatial (vertical and radial) profiles of the electron density and temperature are revealed for different frequency ranges.

1. Introduction

Plasma detachment is thought to be inevitable to control heat load on divertor materials in fusion devices [1]. It is of importance for future fusion devices to elucidate the relevant physics and control the stability of detached plasmas, because the heat load to divertor will easily exceed the limit of water cooled material of $\sim$10 MW/m^2 without any controlling of plasmas [2]. Linear plasma devices have been used for demonstrating detached plasma conditions and contributed to understand the various phenomena relevant to detachment: atomic and molecular processes, convective plasma transport, plasma flow reversal, and so on [3].

Some difficulties arose on measurements of detached plasmas, though diagnostics are crucial for those studies. Electrostatic probes would have an anomalous characteristics [4, 5, 6], probably because of potential fluctuations and an increase in the plasma resistance. Also, spectroscopic measurement requires a modeling of population distribution considering radiation trapping and influence of the transport of metastable atoms in addition to a line integrated issue [7]. Laser Thomson scattering (LTS) is a powerful measurement tool without any disturbances and has been installed in several linear devices. TV Thomson scattering systems, which use a charge coupled device (CCD), an image intensifier, and the second harmonic of Nd:YAG laser (532 nm), were used in Pilot-PSI [8], MAGNUM-PSI, [9], MAP-II [10], PSI-2 [11], and NAGDIS-II [12], while in GAMMA 10 [13], polychromator with the fundamental wavelength of Nd:YAG laser (1064 nm) was used. Although LTS has a disadvantage that temporal evolution measurements are not easily performed, usage of special techniques can overcome the issue. A pulse burst laser system was applied to the MST reversed-field pinch to record the dynamic evolution of the electron temperature profiles [14]. Hubeny *et al* demonstrated turbulence measurement using LTS with a combination of conditional average (CA) in the linear plasma device PSI-2 [11].

Plasma detachment is accompanied by strong plasma recombination, which occurs only in very low temperature plasmas, i.e. $<$2-3 eV for molecular activated recombination (MAR) and $\ll$1 eV for electron ion recombination (EIR), namely radiative and three body recombinations. It has been revealed from linear devices that fluctuations were significantly enhanced in the recombining plasmas and radially broaden the plasma profile [15, 16]. The profile broadening was likely because of an enhancement of radial transport by forming radially elongated spiral plasma structures [17]; similar behavior was demonstrated using three-dimensional global drift fluid simulations [18]. Fast framing camera observation [19], segmented electrode target, and microwave interferometer [20] have been used to investigate the instabilities of the recombining plasmas in the NAGDIS-II. It was found that $m = 0$, 1 instability, where m is the mode number in the azimuthal direction, likely related to the formation of the spiral shaped structures deeply. However, local and absolute measurements of the plasma parameters related with the instabilities have yet to be conducted especially around the central region of the plasma column.

In this study, we will apply CA to LTS measurement of the recombining plasmas in the NAGDIS-II device, where the temperature is in the range of 0.1-1 eV. After presenting measurement results of time averaged plasma parameters using the LTS, we show time evolutions of the electron density, n_e, and temperature, T_e, deduced by CA. We use filtering technique to extract specific phenomena related to fluctuations in the detached recombining plasmas. The LTS will clearly capture the two-dimensional structures of fluctuations. Effects of the fluctuations in n_e and T_e on plasma recombination and plasma diagnostics will be discussed.

2. Methods

2.1. Experimental setup

Experiments were conducted in the linear divertor simulator NAGDIS-II [21], where high density plasmas can be produced in a steady state. In this study, to focus on instabilities that occur in EIR plasmas, pure helium (He) plasma was used. The magnetic field strength was 0.1 T. Figure 1(a) shows a schematic of the experimental setup. An LTS system was developed in the downstream of the plasma column at 16 cm away from the end target. The LTS system used a second harmonic pulsed Nd:YAG laser (Continuum, Surelite II-10) for the light source. The pulse width, the pulse energy, and the repetition rate were ∼5 ns, 0.3 J, and 10 Hz, respectively. The scattered photons from electrons were collected by an optical fiber bundle via a doublet lens, and the photons were transferred to a spectrometer, which uses two photographic lens (300 mm f/2.8 for collimator lens and 200 mm f/2 for focusing lens) and a holographic grating; a charge coupled device (CCD) with a Gen III type image intensifier (Andor, iStar) was used for the detector. Details of the LTS system can be found elsewhere [12, 22]. In Fig, 1(b), a typical CCD image of an LTS signal is shown. The fiber bundle has 21 channels as excluding 2 broken fibers, and radial profile up to ∼15 mm can be obtained without changing the position of the bundle. The values were interpolated at the positions where fibers were broken when deducing the radial profiles. An electrostatic probe was positioned at 16 cm upstream from the LTS location and was used to measure the ion saturation current, which was used as a reference signal for CA. The radial position of the electrostatic probe was several mm away from the center considering the disturbance of the probe, which was revealed recently from a comparison to LTS in an upstream region of the NAGDIS-II device [23].

In the second half of section 3.3, to observe the plasma two dimensionally, we shifted the plasma column vertically by controlling the magnetic field locally. We installed Permalloy (nickel iron magnetic alloy) bars below the vacuum vessel in the LTS measurement region. The position of the plasma column could be shifted toward the direction where Permalloy was located. The amount of the vertical shift, Δy, which was assessed with an electrostatic probe, was controlled by changing the number of the Parmalloy bars and was -5.4 mm in maximum. The vertical position of the referenced

probe was aligned to the center of the column for different Δy values as observing the ion saturation current.

2.2. Conditional average

To apply CA to LTS signals, 10000 LTS signals (frames) were taken without any averaging at first. At the same time, as shown in Fig. 1(b), being synchronized with the LTS measurement, the oscilloscope recorded the ion saturation current of the electrostatic probe, $I_{\rm sat}$, 1000 μs before and after the trigger signal. From the limitation of the data acquisition time, the measurements of the probe and LTS signals were conducted at 1 Hz, and it took ∼3 hours to obtain the necessary data. Figure 2(a,b) shows typical time evolution of I_{sat} and normalized probability density function (PDF) of I_{sat}, respectively. In Fig. 2(a), the LTS signal was taken at $t = 0$ s. The sampling frequency of I_{sat} was 1 μs. The black, red, and blue dotted lines correspond to the average value and positive/negative thresholds used for CA, respectively. Only the peaks that located higher/lower than the positive/negative threshold values are used for CA. The threshold values were chosen from the values where the cumulative PDF reached 10 and 90%, respectively; $\mu_I + 1.3 \times \sigma_I$ for positive peaks and $\mu_I - 1.0 \times \sigma_I$ for negative peaks, where μ_I and σ_I are the averaged value and the standard deviation of $I_{\rm sat}$, respectively. Using the peak times of the ion saturation current, $t_{\rm peak}$, the CA time frame is defined as $\tau = t - t_{\rm peak}$, where the time, t, is defined from the timing of the LTS measurement. We used the data within $-250 < \tau < 250$ μs; if more than one peak was found in the time range, we used the LTS signal multiple times for all the peaks. In Fig. 2(a), the timings of four peaks exceeded the threshold were represented with arrows. E.g., considering the maximum peak at ∼-110 μs, the timing of the LTS signal corresponds to 110 μs from the event identified in the reference probe signal. In the same manner, t_{peak} was determined for all the peaks identified on the collected 10000 signals. The LTS signals corresponded to all the peaks were rearranged in the time frame of τ, and the LTS signal was averaged with an averaging time window of 5 μs. Roughly, 200-500 signals were used to deduce an LTS spectrum for each time window.

Figure 3 shows a fast Fourier transform (FFT) power spectrum of $I_{\rm sat}$. In addition to a broad peak around 6 kHz, a major peak appeared at ∼24 kHz. We also used filtered reference signal for CA to extract the phenomena in different frequency domains. Tanaka *et al* discussed from fluctuation analysis using a segmented electrode target and microwave interferometer that the two peaks corresponded to ejections and rotations of radially elongated spiral plasma structure, respectively, and that the frequency could be altered by changing the plasma parameters. Because the 6 and ∼24 kHz peaks likely corresponded to the ejections and rotations of plasmas, respectively, we used the negative threshold for 6 kHz and positive threshold for 24 kHz.

3. Results

3.1. LTS measurements

Figures 4(a,b) show LTS spectra at 5.1 and 15.7 mTorr, respectively, at the center of the plasma column. Since stray light overlaps the LTS signal in the center of the spectrum [12], the central region of the spectrum, roughly the width of 1.2-1.3 nm, was eliminated for fitting similar to other devices [10, 9]. The spectrum can be well fitted by a single Gaussian function (gray lines) in Fig. 4(a), while tail part is clearly deviated from single Gaussian fitting in Fig. 4(b). Firstly, an overview of the pressure dependences of profiles are shown without considering the deviation from the single Gaussian fittings. Figures 5(a,b) show pressure, P, dependences of n_e and T_e profiles deduced from LTS. The discharge current was 60 A, and the contour plots were made from the measurements conducted at 5.1, 6.9, 8.9, 9.4, 11.6, and 15.7 mTorr with a radial resolution of ∼0.9 mm. With increasing the pressure, n_e increased, had a peak value of 1.9×10^{19} m^{-3} around ∼9 mTorr, and decreased when P was higher, while T_e decreased from ∼ 3 to 0.2-0.3 eV gradually. The density rollover, which was caused by plasma recombination, led to the rollover of the plasma particle flux, which is regarded as the manifestation of plasma detachment [24].

In Fig. 4(a,b), double Gaussian fitting results are shown with blue and red dotted lines for low and high temperature components, respectively. At 5.1 mTorr, the low T_e component was much smaller than the high T_e component or single Gaussian result, showing that the single Gaussian fit was almost enough to explain the energy distribution function. Using double Gaussian function, the tails around 530/540 nm are well explained. However, the signal level seemed significantly greater than the noise level even around 527/537 nm, indicating that higher energy components exist. Although it cannot perfectly describe the LTS spectrum, we use double Gaussian function for fitting to see the overview of the energy distribution function more clearly than the single Gaussian profiles shown in Fig. 5. Figures 6(a,b) present pressure dependences of n_e and T_e at the center of the plasma column. Here, the densities of high and low temperature components are expressed as n_{H} and n_{L}, respectively. Figure 6(c) shows the pressure dependence of the density ratio of the low temperature component to both the components, i.e. $n_{\mathrm{L}}/(n_{\mathrm{H}}+n_{\mathrm{L}})$. When the pressure was ∼5 mTorr, the predominant component was the high temperature one (3 eV), and the low temperature component (0.6 eV) was less than 10%. The fraction of the low temperature component increases with the pressure and almost reached 80% when P was 16 mTorr, while the temperatures of the both components decreased gradually.

It was shown using a particle-in-cell simulation that non-Maxwellian features were pronounced especially in high-recycling regimes due to non-local mean-free path effects [25]. The non-Maxwellan component can be important to understand atomic and molecular processes, because it will change the various rate coefficients that require high energies such as ionization processes [1]. In addition to the mean-free path effects, we suspected that the high energy component was related to the temporal evolution of T_e

and/or n_e, because the plasma fluctuation increased significantly when the plasma was changed from attached to detached plasmas [15]. In section 3.2, the temporal evolutions of n_e and T_e are shown based on the CA technique.

3.2. Conditional average

Figure 7(a) shows $I_{\rm sat}$ as a function of τ obtained from CA method. Here, positive threshold was used with no filtering for the reference signal. The discharge current was 60 A and the neutral pressure was 15 mTorr. In addition to a strong peak at $\tau = 0$ μs, small ripples with a time interval of $\sim$40 μms can be identified. Figures 7(b-d) show the time evolution of $n_e\sqrt{T_e}$, n_e, and T_e obtained from LTS. Here, $n_e\sqrt{T_e}$ is shown because it is proportional to the ion saturation current shown in Fig. 7(a). It is noted that single Gaussian function was used for fitting here, because the error would be too large to discuss the temporal evolution with two temperature components. Similar to $I_{\rm sat}$, $n_e\sqrt{T_e}$ had a peak at $\tau = 0$ μs, and small ripples appeared with an interval of $\sim$ 40 μs, e.g., at $\sim$-120, 30, and 130 μs, where peaks were identified on $I_{\rm sat}$ as well. The results suggested that the LTS deduced consistent value with the electrostatic probe. In a similar manner, clear peaks can also be identified on n_e and T_e at $\tau = 0$ ms. The density increased from 6×10^{18} to 8×10^{18} m^{-3} by $\sim$ 30%, and the temperature increased from 0.35 to 0.65 eV by almost double. One can say that both increases in n_e and T_e contributed to the increase in $I_{\rm sat}$. The increase in T_e is likely one of the important mechanisms to produce the non-Maxwellian component appeared in time averaged spectra shown in Fig. 4(b).

Figure 8 shows time averaged n_e and T_e deduced from single and double Gaussian fitting procedures using the same data in Fig. 7. At $x > 10$ mm, the low temperature component was predominant, while the fraction of the high temperature component increased with decreasing the radial position and was $\sim$40% at the center of the plasma column. At $x > 10$ mm, no clear fluctuation was identified, and the temperature was less than 0.2 eV, as was in Figs. 7(c,d), suggesting that averaged and time resolved values were consistent with each other. On the other hand, around the center, the temperatures of high and low T_e components were 0.8 and 0.2 eV, respectively, which were slightly higher and lower than the temperature variation identified in Fig. 7(d), where the temperature altered from 0.35 to 0.65 eV at the center. The variation in T_e could be altered if different threshold value was used. The present study used single Gaussian fitting for CA because only 200-500 data in each time slice for average were not enough to discuss the deviation of single Gaussian function. It is of interest to investigate the non-Maxwellian component using conditional averaged spectra for future by increasing the time window or data acquisition time.

3.3. CA with filtering

We apply filters to the reference signal $I_{\rm sat}$ to focus on the process that occurred at different frequency ranges. As was discussed in section 2.2, the negative and

positive thresholds were applied for the low (<12 kHz) and high frequency (20-30 kHz) components, respectively. Figures 9(a-c) show the conditional averaged I_{sat}, n_e, and T_e, respectively, for < 12 kHz components with the negative threshold. A slight temperature increase is followed by a clear density increase, which has a peak at ∼60 μs before the negative peak. During the negative peak in $I_{\rm sat}$, the density and temperature were dropped together. The density and temperature recovered to the initial values after a peak around 50 μs. In this frequency range, n_e and T_e fluctuated even at the center without any higher modes in azimuthal direction, indicating that $m = 0$ mode was the major instability.

Figures 9(d-f) show I_{sat}, n_e, and T_e, respectively, as a function of τ for 20-30 kHz component; the positive peak threshold was used for CA. In addition to I_{sat}, n_e and T_e also have peaks with an interval of 40 μs. A detailed look at Fig. 9 reveals that the peak region is slightly ($\sim 8°$, which corresponds to ∼700 m/s) tilted clockwise direction, indicating that structure moves from positive to negative x direction.

3.4. Vertical profiles

We shifted the vertical position of the plasma as described in section 2.1 to see how the plasma motion alters. Figure 10(a-c) shows temporal evolution of $n_e\sqrt{T_e}$ at different Δy: (a) $\Delta y = 0$, (b) $\Delta y = -3.0$, and (c) $\Delta y = -5.4$ mm. The clockwise tilt identified at $y = 0$ becomes not apparent when $\Delta y = -3.0$ mm, and the peaks appear at ± 2-3 mm alternately. Moreover, it seems that a slight anti-clockwise tilting appears when $\Delta y = -5.4$ mm. The clockwise tilting meant that the dense plasma region moved from $x = 3$ to -3 mm in $-x$ direction; the anti-clockwise tilting corresponded to motion of the high dense plasma region in $+x$ direction. With decreasing Δy (shifting the plasma downward), the measurement position relatively moves upward as the laser position was fixed. Thus, Figs. 10(a-c) illustrated that the motion of the dense region changed from $-x$ direction to $+x$ direction with increasing the relative measurement position to the plasma. Moreover, it was likely that actual center of the plasma column was measured at $\Delta y = -3.0$ mm from the fact that dens plasma region appeared symmetrically in x direction at $\Delta y = -3.0$ mm. The LTS measured a lower part of the plasma column at $\Delta y = 0$ mm, while a slightly upper part of the plasma column was seen at $\Delta y = -5.4$ mm.

Figure 10(d) shows a schematic representing the configuration of the rotating plasma and the measurement position seen from the source region. Because the potential has a well-shaped profile, the direction of the electric field is always inward direction, and the plasma rotates in clockwise direction by $\boldsymbol{E} \times \boldsymbol{B}$ drift. The measurement results suggested that the dens plasma region rotated in $\boldsymbol{E} \times \boldsymbol{B}$ direction. The rotating plasma moved to $-x$ direction in the lower half, whereas it moved to $+x$ direction in the upper half.

To focus on the temporal variation, the averaged value was subtracted from Fig. 10(b), and the temporal variation of $n_e\sqrt{T_e}$ in 20-30 kHz frequency range from LTS

signals is shown in Fig. 11. The major variation occurs in the region of $x = 2 - 8$ mm; the variation around the center ($x < 2$ mm) is smaller than the surrounding area. The peak in the positive and negative x appeared one after the other in a period of $\sim$40 μs. It is confirmed that the temporal variation is due to the plasma rotation.

4. Discussion

This is the first time that the variations of n_e and T_e in response to plasma instability in detached plasmas were observed in a detailed manner with a high time resolution. It is worthwhile to note the importance of the observed fluctuations of n_e and T_e in the recombining detached plasmas. In the present situation, the major recombination processes are following three body and radiative recombination processes:

$$\mathrm{He}^+ + 2e^- \rightarrow \mathrm{He} + e^-, \tag{1}$$

$$\mathrm{He}^+ + e^- \rightarrow \mathrm{He} + h\nu. \tag{2}$$

For the three body recombination, because the rate coefficient is strongly depend on T_e and n_e, a slight variations in the parameters could significantly change the reaction.

The temperature dependence of the recombination rate is very strong. Figure 12(a) shows temperature dependences of the collisional radiative recombination rate coefficient α_{CR}, which includes radiative, three body and dielectric recombinations, calculated at $n_e = 10^{18}$ and 10^{19} m^{-3} using a helium collisional radiative (CR) model [26]. The recombination rate coefficient was deduced by solving set of rate equations, and the recombination flux can be expressed as $\alpha_{\mathrm{CR}} n_i n_e$. In the CR model, the neutral pressure was assumed to be the experimental condition of 15 mTorr, and the radiation trapping was taken into account using an optical escape factor (OEF) with the OEF radius of 25 mm, the validity of which was investigated previously [27, 28]. The recombination rate increases by two orders of magnitude with decreasing the temperature from 1 to 0.1 eV. When $n_e = 10^{19}$ m^{-3}, α_{CR} alters by a factor of five in the temperature range of 0.3-0.6 eV.

To consider the effect of recombination quantitatively, an assessment of the recombination flux, which is the number of recombination events per unit volume per second [29], is important. Considering that $n_e = n_i$ can be assumed in this study, the recombination flux has a n_e^2 dependence without considering the n_e dependence of α_{CR}, which also increases with n_e, as shown in Fig 12(a). Thus, the recombination flux has non-linear dependences both on n_e and T_e. The averaged n_e and T_e are usually used to assess the recombination flux. However, because of the non-linearity, the recombination flux assessed from the averaged values can be different from the actual recombination flux considering the time evolution.

Figure 12(b) shows the time evolutions of the recombination flux for the high and low frequency filter cases shown in Figs. 9(a-c) and (d-f), respectively. For the high frequency case, the recombination flux fluctuated at $\sim$ 25 kHz, and the minimum and maximum values differed by a factor of three; moreover, the time variations was greater

for the low frequency case. In the range of -30 to 60 μs, the recombination flux increased significantly by a factor of two to eight from the averaged value, mainly because of the decrease in T_e. When using the averaged n_e and T_e, the recombination rate was 1.5×10^{20} m^{-3}s^{-1} for the low frequency filter case and 1.3×10^{20} m^{-3}s^{-1} for the high frequency filter case. Averaged values can differ when average is taken considering the temporal variation. The recombination rate became 1.3×10^{20} m^{-3}s^{-1} for the low frequency filter case and 1.9×10^{20} m^{-3}s^{-1} for high frequency filter case after considering the time evolution. The recombination flux was underestimated by more than 40% for the low frequency filter case. The 40% difference could have a significant impact on the heat load on the material in fusion devices, since the recombination flux is directly related to the heat load.

In addition to the effect on the recombination flux, the time evolution can be influential on the plasma diagnostics as well. Helium atomic line intensities have been used to measure n_e and T_e with the help of the population distribution modeling using a CR model. The method is called the line intensity ratio method. In this method, a set of n_e and T_e that minimized the difference between the modeling and measured line intensities is chosen to be the plasma parameters; in other words, a set of n_e and T_e is deduced by solving an inverse problem to realize the observed emissions. However, because emission intensities have also non-linear relation with T_e in particular, a difficulty could appear when using time averaged emission intensities. Recently, it was shown that two solutions appeared when solving the inverse problem in detached recombining plasmas in particular [7]; it was discussed that one of the reason could be the time evolution in n_e and T_e.

Time resolved measurements are inevitable to solve those issues; it is not easy to find reliable local and time resolved measurements in detached plasmas. It was confirmed in this study that LTS can be a powerful time resolved measurement method with the help of CA for qualitative assessment and further understanding of detached plasmas. For example, in this study, the reference probe was almost at the center of the plasma column and instabilities occurred inside were focused. Thus, it is of interest to put the reference probe at the peripheral region of the plasma column to observe relevant phenomena to ejection of blob-like plasma structures.

5. Conclusions

In this study, laser Thomson scattering (LTS) measurement was conducted in detached recombining helium plasmas in the divertor simulator NAGDIS-II. When the neutral pressure was increased from 5 to 15 mTorr, n_e increased up to $\sim$9 mTorr and started to decrease when the pressure was higher, while the temperature dropped gradually from 3 to 0.2-0.3 eV; The rollover of n_e suggested the manifestation of plasma detachment by recombination processes. When increasing the neutral pressure, it was found in LTS spectra cannot be fitted well with a single Gaussian function especially in the tail part, suggesting that the electron distribution function had a non-Maxwellian component.

We obtained the two components, i.e. hot and cold components, using double Gaussian fitting procedure. At 5 mTorr, the hot component was predominant one; the cold component increased gradually with increasing the pressure and became comparable to the hot component around 10 mTorr, where the density peaked.

Conditional averaging technique was applied to LTS spectra to obtain the time evolution of n_e and T_e using the ion saturation current of an electrostatic probe as a reference signal. Increases in n_e and T_e were identified when the reference signal had a peak. The results suggested that the time variation in T_e could be one of the important factor to cause the non-Maxwellian electron energy distribution function (EEDF). However, the range of the time variation in T_e was slightly smaller than the high and low temperature components obtained from the double Gaussian fitting. It is of interest to measure the variation in EEDF using the conditional averaged data in future by improving the data quality.

We extracted two different structures by applying frequency filters (low frequency: <12 kHz and high frequency: 20-30 kHz) to the reference signals. For the low frequency case, increases, followed by drops and increases in the density and temperature were identified. It was found that $m = 0$ mode was predominant component in this frequency range. In the high frequency case, motion of structures in transversal direction was identified. As changing the vertical position of the plasma column, 2D structures of the motion of the structure were anatomized. As a result, a rotation of high density region in $\boldsymbol{E} \times \boldsymbol{B}$ direction was observed when the laser beam passed through the center of the plasma column. It is likely that the low frequency $m = 0$ instability and the high frequency plasma rotation are related to the ejection of radially elongated spiral plasma structures previously identified in the NAGDIS-II device [17]. In this study, we focused on the instability occurred at the center of the plasma column as positioned the reference probe around the center. Thus, it was difficult to see the phenomena related to the ejected plasma structures. For future work, it is of important to investigate the phenomena by focusing on the ejected structures using the reference signal at the periphery of the plasma column.

Concerning the observed density and temperature fluctuations, drift wave and/or flute instabilities, which have been observed in linear devices [30], are the candidate mechanisms. For both of the instabilities, the radial potential profile is an important parameter [31]; it is of interest to discuss the mechanism of the instability further in future with detailed potential measurements.

6. Acknowledgement

The authors appreciate useful discussion and technical help from Dr. Hennie van der Meiden from DIFFER. This work was supported in part by a Grant-in-Aid for Scientific Research 15H04229, 16H02440, and 16H06139, Grant-in-Aid for Exploratory Research 16K13917, Fund for the Promotion of Joint International Research 17KK0132 from the Japan Society for the Promotion of Science (JSPS), JSPS Bilateral Joint

Research Project, and the NIFS Collaboration Research program (NIFS17KUGM120 and NIFS17KUGM130).

[1] S. I. Krasheninnikov and A. S. Kukushkin 2017 Journal of Plasma Physics **83** 155830501.
[2] A. Herrmann 2002 Plasma Physics and Controlled Fusion **44** 883.
[3] N. Ohno 2017 Plasma Physics and Controlled Fusion **59** 034007.
[4] R. D. Monk, A. Loarte, A. Chankin, S. Clement, S. J. Davies, J. K. Ehrenberg, H. Y. Guo, J. Lingertat, G. F. Matthews, M. F. Stamp and P. C. Stangeby 1997 J. Nucl. Mater. **241-243** 396.
[5] N. Ezumi, N. Ohno, K. Aoki, D. Nishijima and S. Takamura 1998 Contrib. Plasma Phys. **38** S31.
[6] S. Kado, Y. Iida, S. Kajita, D. Yamasaki, A. Okamoto, B. Xiao, T. Shikama, T. Oishi and S. Tanaka 2005 Journal of Plasma Fusion Research **71** 810.
[7] S. Kajita, K. Suzuki, H. Tanaka and N. Ohno 2018 Physics of Plasmas **25** 063303.
[8] H. J. van der Meiden *et al.* 2008 Review of Scientific Instruments **79** 013505.
[9] H. J. van der Meiden *et al.* 2012 Review of Scientific Instruments **83** 123505.
[10] F. Scotti and S. Kado 2009 J. Nucl. Mater. **390-391** 303.
[11] M. Hubeny, B. Schweer, D. Luggenholscher, U. Czarnetzki and B. Unterberg 2017 Nuclear Materials and Energy **12** 1253 .
[12] S. Kajita, T. Tsujihara, M. Aramaki, H. van der Meiden, H. Oshima, N. Ohno, H. Tanaka, R. Yasuhara, T. Akiyama, K. Fujii and T. Shikama 2017 Physics of Plasmas **24** 073301.
[13] M. Yoshikawa *et al.* 2015 Fusion Science and Technology **68** 99.
[14] D. J. Den Hartog, J. R. Ambuel, M. T. Borchardt, A. F. Falkowski, W. S. Harris, D. J. Holly, E. Parke, J. A. Reusch, P. E. Robl, H. D. Stephens and Y. M. Yang 2010 Review of Scientific Instruments **81** 10D513.
[15] N. Ohno, V. Budaev, K. Furuta, H. Miyoshi, and S. Takamura 2004 Contrib. Plasma Phys. **44** 222.
[16] E. M. Hollmann, C. Brandt, B. Hudson, D. Kumar, D. Nishijima and A. Y. Pigarov 2013 Physics of Plasmas **20** 093303.
[17] H. Tanaka, N. Ohno, Y. Tsuji and S. Kajita 2010 Contributions to Plasma Physics **50** 256.
[18] D. Reiser, N. Ohno, H. Tanaka and L. Vela 2014 Physics of Plasmas **21** 032302.
[19] S. Kajita, H. Tanaka, N. Ohno and T. Onda 2018 Plasma and Fusion Research **13** 1402033.
[20] H. Tanaka, K. Takeyama, M. Yoshikawa, S. Kajita, N. Ohno and Y. Hayashi 2018 Plasma Physics and Controlled Fusion **60** 075013.
[21] N. Ohno, D. Nishijima, S. Takamura, Y. Uesugi, M. Motoyama, N. Hattori, H. Arakawa, N. Ezumi, S. Krasheninnikov, A. Pigarov and U. Wenzel 2001 Nucl. Fusion **41** 1055.
[22] H. Ohshima, S. Kajita, H. Tanaka, N. Ohno and H. J. van der Meiden 2018 Plasma and Fusion Research **13** 1201099.
[23] H. Takano, H. Ohshima, S. Kajita, H. Tanaka and N. Ohno 2019 Plasma Fusion Research **14** 2405031.
[24] S. I. Krasheninnikov, A. S. Kukushkin and A. A. Pshenov 2016 Physics of Plasmas **23** 055602.
[25] O. V. Batishchev, S. I. Krasheninnikov, P. J. Catto, A. A. Batishcheva, D. J. Sigmar, X. Q. Xu, J. A. Byers, T. D. Rognlien, R. H. Cohen, M. M. Shoucri and I. P. Shkarofskii 1997 Physics of Plasmas **4** 1672.
[26] M. Goto 2003 J. Qunantitative Spectroscopy and Radiative Transfer **76** 331.
[27] S. Kajita, N. Ohno, S. Takamura and T. Nakano 2006 Phys. Plasmas **13** 013301.
[28] S. Kajita, N. Ohno, S. Takamura and T. Nakano 2009 Physics of Plasmas **16** 029901.
[29] M. Goto, K. Sawada and T. Fujimoto 2002 Physics of Plasmas **9** 4316.
[30] K. Kamataki, Y. Nagashima, S. Shinohara, Y. Kawai, M. Yagi, K. Itoh and S.-I. Itoh 2007 Journal of the Physical Society of Japan **76** 054501.
[31] M. Yoshinuma, M. Inutake, R. Hatakeyama, T. Kaneko, K. Hattori, A. Ando and N. Sato 1999 Physics Letters A **255** 301 .

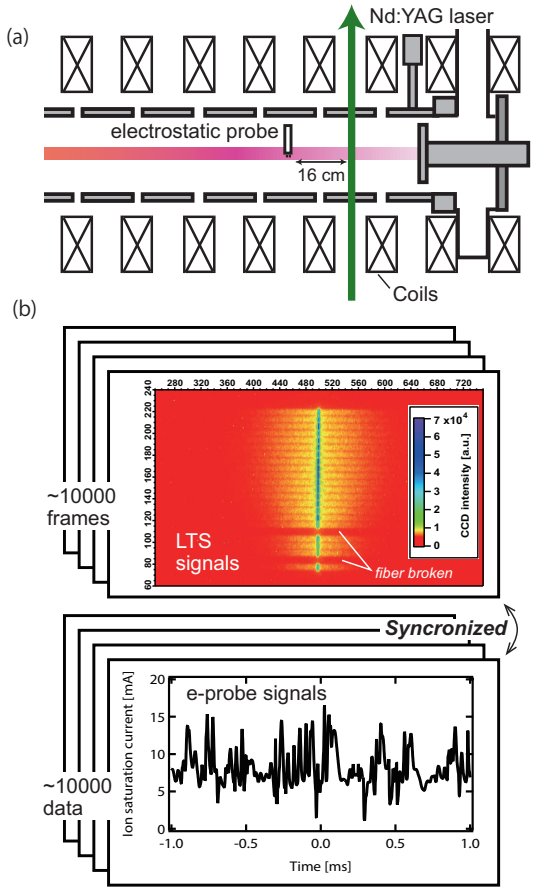

Figure 1. (a) A schematic of the experimental setup and (b) a diagram to explain CA with temporal evolutions of the ion saturation current and LTS signal images.

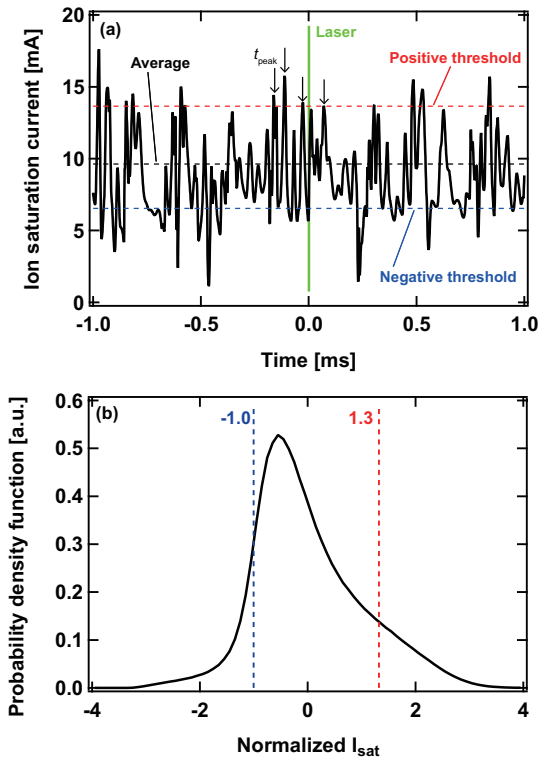

Figure 2. (a) Typical time evolution of I_{sat} and (b) normalized probability density function (PDF) of I_{sat}. The black, blue, and red dotted lines correspond to averaged value, threshold value for positive peaks, and for negative peaks, respectively.

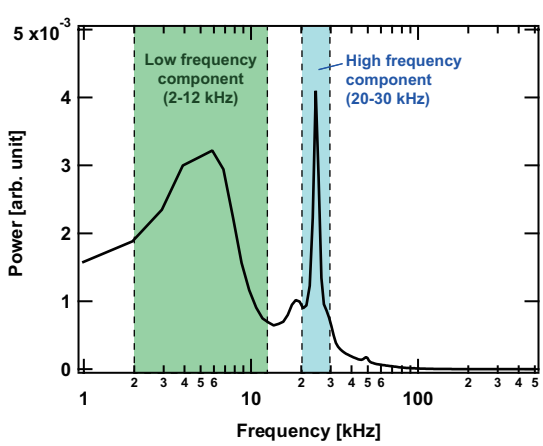

Figure 3. An FFT power spectrum of I_{sat}.

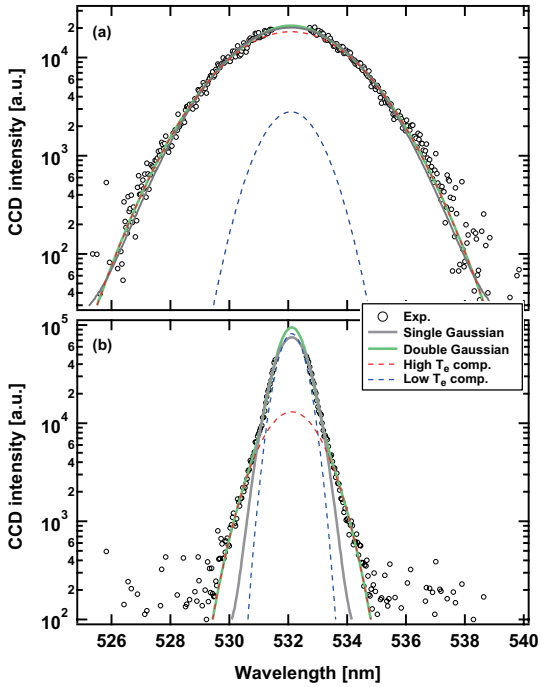

Figure 4. LTS spectra at (a) 5.1 and (b) 15.7 mTorr, respectively, at the center of the plasma column. Double Gaussian function is used for fitting procedure in addition to single Gaussian.

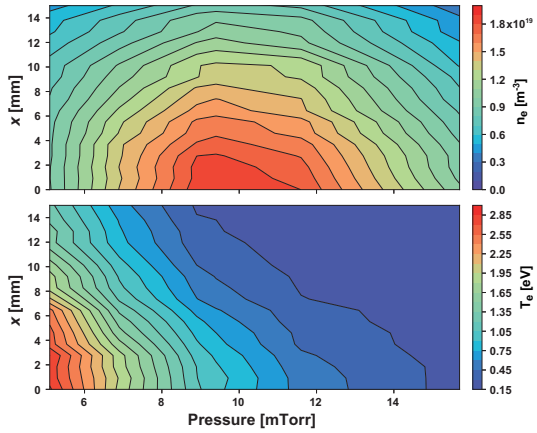

Figure 5. Pressure dependences of n_e and T_e profiles deduced from LTS. The measurements conducted at 5.1, 6.9, 8.9, 9.4, 11.6, and 15.7 mTorr with a radial resolution of ∼0.9 mm.

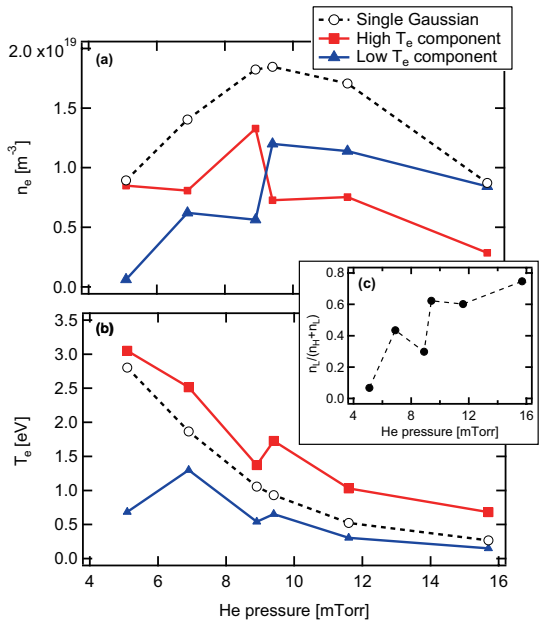

Figure 6. Pressure dependences of n_e and T_e deduced from LTS. In addition to single Gaussian fitting results, high and low temperature components obtained from double Gaussian fittings are shown.

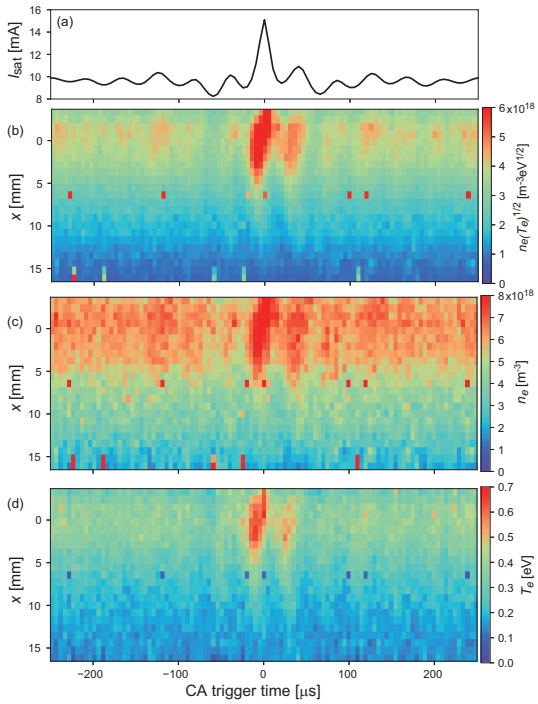

Figure 7. Time evolutions of (b) $n_e\sqrt{T_e}$, (c) n_e, and (d) T_e profiles measured by LTS with CA using the reference signal of the ion saturation current shown in (a).

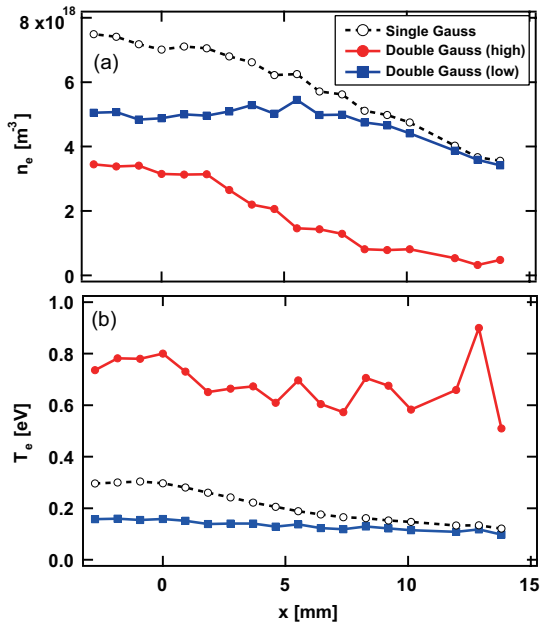

Figure 8. Time averaged radial profiles of (a) n_e and (b) T_e deduced from single and double Gaussian fitting procedures.

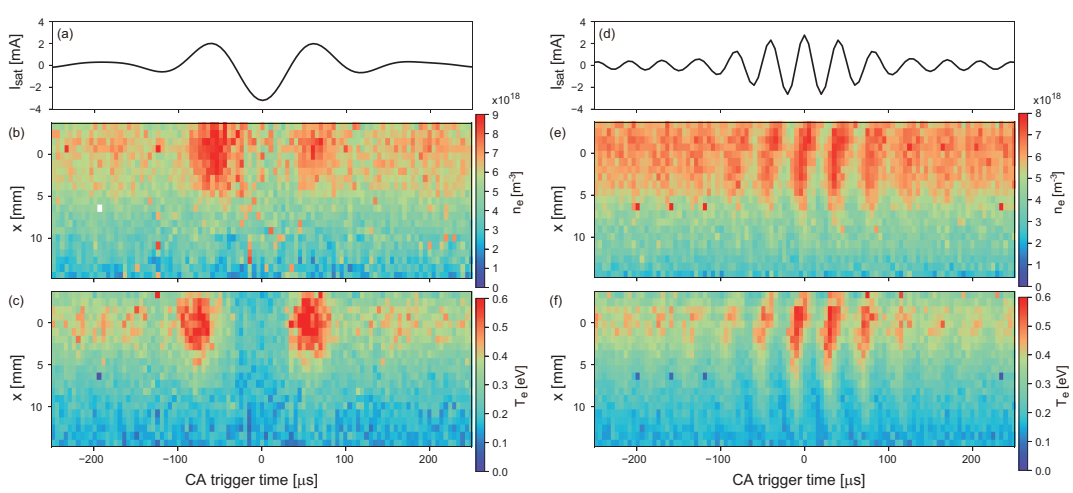

Figure 9. Time evolutions of the radial profiles of (a,d) the ion saturation current, (b,e) n_e and (c,f) T_e measured by LTS with CA using frequency filters. The frequency ranges were (a-c) < 12 and (d-f) 20-30 kHz.

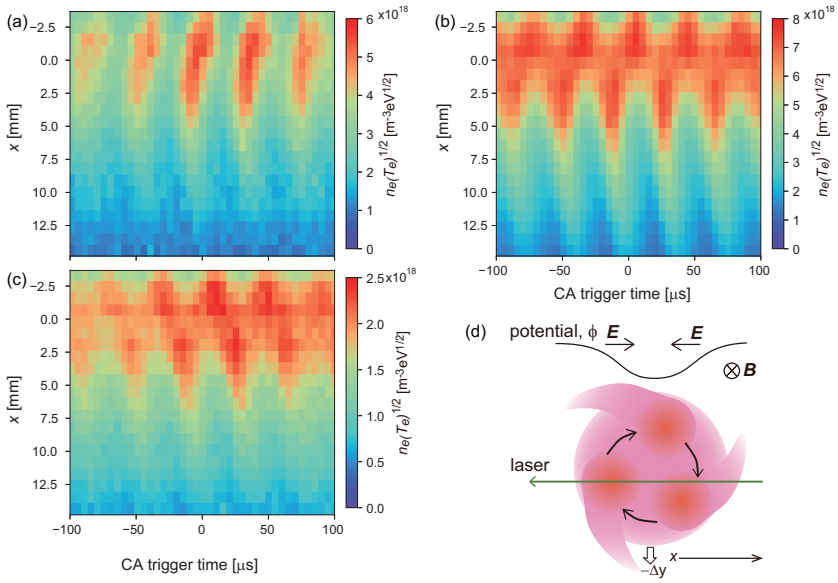

Figure 10. (a-c) Time (τ) evolution of $n_e\sqrt{T_e}$ with a frequency filter of 20-30 kHz range at different Δy and (d) a schematic representing the measurement position and the plasma rotation.

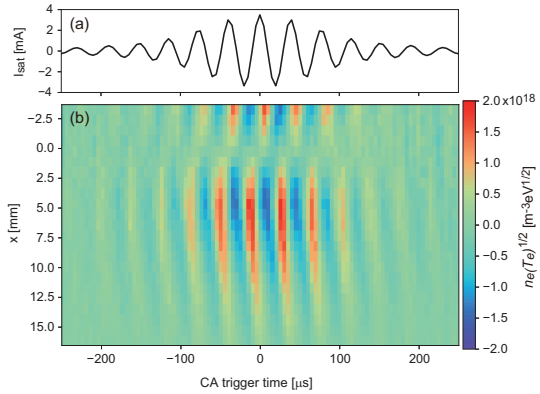

Figure 11. Temporal variation of $n_e\sqrt{T_e}$ in 20-30 kHz frequency range obtained CA LTS signals at $\Delta y = 3.0$ mm.

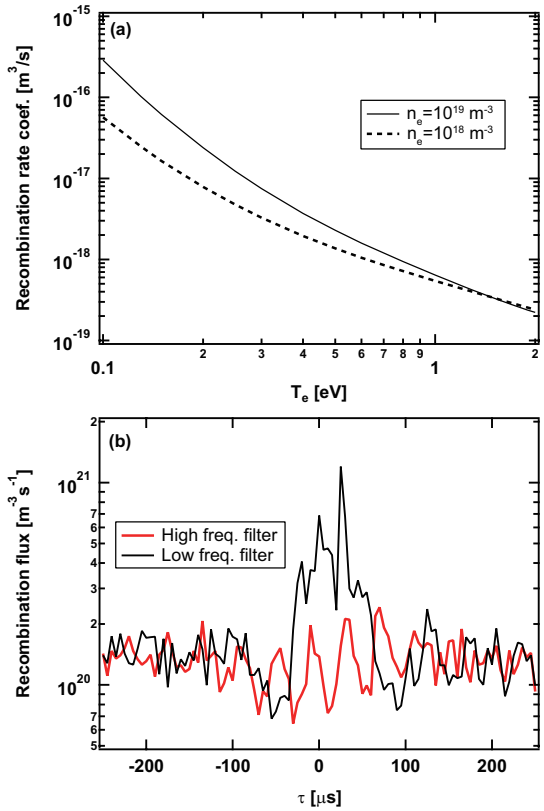

Figure 12. (a) Temperature dependence of the collisinal radiative recombination rate coefficient at $n_e = 10^{18}$ and 10^{19} m^{-3}, and (b) recombination flux as a function of τ for high and low frequency filter cases shown in Fig. 9.